Sun, L., Xu, J., Xiong, C., Zhu, Y., Yuan, W., Hu, L., Liu, W., Chen, G. (2019): Midlatitudinal Special Airglow Structures Generated by the Interaction Between Propagating Medium-Scale Traveling Ionospheric Disturbance and Nighttime Plasma Density Enhancement at Magnetically Quiet Time. - *Geophysical Research Letters*, *46*, 3, pp. 1158—1167.

DOI: http://doi.org/10.1029/2018GL080926

Geophysical Research Letters

RESEARCH LETTER
10.1029/2018GL080926

Key Points:
- MSTID with a poleward surged airglow depletion/enhancement and a bifurcation of depletion occurred during the magnetically quiet time
- Secondary gradient drift instability could have developed the poleward surged bifurcation of depletion
- This event is suggested to be caused by the interaction between MSTID and NPDE

Supporting Information:
- Supporting Information S1
- Movie S1
- Movie S2
- Movie S3

Correspondence to:
L. Sun,
lcsun@spaceweather.ac.cn

Citation:
Sun, L., Xu, J., Xiong, C., Zhu, Y., Yuan, W., Hu, L., et al. (2019). Midlatitudinal special airglow structures generated by the interaction between propagating medium-scale traveling ionospheric disturbance and nighttime plasma density enhancement at magnetically quiet time. *Geophysical Research Letters*, *46*, 1158–1167. https://doi.org/10.1029/2018GL080926

Received 15 OCT 2018
Accepted 22 JAN 2019
Accepted article online 28 JAN 2019
Published online 10 FEB 2019

Midlatitudinal Special Airglow Structures Generated by the Interaction Between Propagating Medium-Scale Traveling Ionospheric Disturbance and Nighttime Plasma Density Enhancement at Magnetically Quiet Time

Longchang Sun[1], Jiyao Xu[1,2], Chao Xiong[3], Yajun Zhu[4], Wei Yuan[1], Lianhuan Hu[5], Weijun Liu[1], and Gang Chen[6]

[1]State Key Laboratory of Space Weather, National Space Science Center, Chinese Academy of Sciences, Beijing, China, [2]University of Chinese Academy of Sciences, Beijing, China, [3]Helmholtz Centre Potsdam, GFZ German Research Center for Geosciences, Postsdam, Germany, [4]Institute of Energy and Climate Research (IEK-7), Forschungszentrum Juelich GmbH, Juelich, Germany, [5]Key Laboratory of Earth and Planetary Physics, Institute of Geology and Geophysics, Chinese Academy of Sciences, Beijing, China, [6]School of Electronic Information, Wuhan University, Wuhan, China

Abstract This paper reports a special midlatitudinal medium-scale traveling ionospheric disturbance (MSTID) event, accompanied by a poleward surge of airglow depletion/enhancement and a bifurcation of depletion during the magnetically quiet period. These special structures were generated during a decreasing height of ionosphere with nighttime plasma density enhancement and increment of airglow emission intensity possibly caused by a passing-by midnight brightness wave. We suggest that the interaction of the passing-by MSTID and nighttime plasma density enhancement resulted in the poleward surge and bifurcation of airglow depletion. The nighttime plasma density enhancement could feed the high plasma density to interact with the airglow depletions of MSTID, causing the poleward surge and bifurcation of airglow depletion by the secondary gradient drift instability. The poleward surged airglow enhancement within two adjacent depletions of MSTID is also firstly reported in this study.

Plain Language Summary It was generally believed that the midlatitudinal ionosphere is fairly quiescent until the first report of airglow structure of the medium-scale traveling ionospheric disturbance by Garcia, Kelley, Makela, and Huang (2000, https://doi.org/10.1029/1999JA000305). Kelley et al. (2000, https://doi.org/10.1029/2000GL000022) and Garcia, Kelley, Makela, Sultan, et al. (2000, https://doi.org/10.1029/1999JA000306) further reported magnetically storm-time "intense mid-latitude spread *F*" events accompanied by poleward surged bifurcations of airglow depletions, which caused the severe perturbations of GPS signal. Those two events were most likely the interactive result of airglow depletion and enhanced plasma density region from the equatorial ionization anomaly crest region driven by magnetic storms. In this paper, we report a very similar airglow event accompanied by a poleward surged airglow depletion/enhancement and a bifurcation of depletion but occurred at magnetically quiet time in Xinglong, China. We suggest that the interaction of the passing-by medium-scale traveling ionospheric disturbance and the nighttime plasma density enhancement/nighttime increment of airglow emission intensity from a possible source of midnight brightness wave resulted in the poleward surged bifurcation of aiglrow depletion, most likely driven by the secondary gradient drift instability. This event can broaden our knowledge on the dynamical process of midlatitudinal ionosphere and provide a new guidance for further investigation of the midlatitudinal special airglow events.

1. Introduction

Very few studies (e.g., Garcia, Kelley, Makela, Sultan, et al., 2000; Kelley et al., 2000) reported events accompanied by characteristics of poleward surge and bifurcation in airglow depletions at midlatitudes. Two storm-time events reported by Garcia, Kelley, Makela, Sultan, et al. (2000) and Kelley et al. (2000) were most likely the interactive result of airglow depletion and high plasma density region of the equatorial ionization anomaly (EIA) crest. Eastward perturbation electric fields induced by geomagnetic storms could drive the

secondary gradient drift instability (SGDI) to generate those bifurcations. However, such kind of events, especially those associated with the medium-scale traveling ionospheric disturbance (MSTID), was never reported during the magnetically quiet period. Studies focusing on equatorial plasma blob (or plasma density enhancement) from airglow observations were previously reported by Pimenta et al. (2004, 2007). However, none of these studies has reported poleward surged airglow enhancement within adjacent depletions of MSTID at midlatitudes.

The nighttime plasma density enhancement (NPDE) is another intriguing ionospheric phenomenon that can occur at midlatitudes during both magnetically quiet and disturbed periods. The storm-time NPDE has been attributed to a westward electric field-induced downward vertical drift together with the flux from the plasmasphere (e.g., Park, 1971) or enhancement of poleward neutral wind caused by large-scale traveling ionospheric disturbance (TID; e.g., Shiokawa et al., 2002). A westward electric field (e.g., Liu et al., 2013) or a large-scale TID (e.g., Chen et al., 2018) can be also a source of these anomalous NPDEs at magnetically quiet time. However, there are still some controversial interpretations regarding the quiet-time NPDE (e.g., Chen et al., 2018). Therefore, more studies are encouraged.

The midnight brightness wave (MBW) is an ionospheric phenomenon associated with the midnight temperature maximum (e.g., Colerico et al., 1996. Colerico & Mendillo, 2002). The MBWs frequently occur at the geographic equator, propagating poleward or equatorward and causing a reversal/abatement of meridional neutral winds (e.g., Colerico & Mendillo, 2002). The MBWs can also hold high plasma density to feed or erode the airglow depletions (e.g., Narayanan et al., 2014, 2016; Sun et al., 2017). Thus the MBWs can be a source of NPDE.

In this paper, we report a special airglow event at magnetically quiet time, exhibiting as a poleward surge of airglow depletion/enhancement and a bifurcation of depletion, which was observed by an all-sky airglow imager (ASAI) deployed at Xinglong (40.4°N, 117.6°E; dip latitude: 30.5°N; inclination (I) = 57.7°), China. In this event, the NPDE of the background ionosphere near midnight was also observed by a digisonde located at Shisanling (40.7°N, 116.6°E; dip latitude: 30.7°N). Accompanied by the NPDE is a nighttime increment of airglow emission intensity (NIAEI) that occupies a broad field of view (FoV) of the ASAI (at least 40.0°). This event is considered to be caused by the interaction of the passing-by airglow depletion of MSTID and the NPDE. The MBW is suggested as a possible source of the NPDE and NIAEI. The SGDI could have developed the poleward surged bifurcation of depletion. Another finding of this paper is the poleward surged airglow enhancement within two adjacent depletions of MSTID at midlatitude, which is firstly reported.

2. Observations and Instruments

Instruments used in this study include two ASAIs, an ionospheric digisonde, a Fabry-Perot interferometer (FPI), and a spectrometer. Except for the digisonde, other instruments are parts of the Chinese Meridian Project (Wang, 2010). The MSTID airglow event was observed by the ASAI deployed at Xinglong in 1 January 2012. Airglow observations from another ASAI deployed at Fuke (19.5°N, 109.1°E; dip latitude: 9.5°N) exclude this MSTID from the equatorial plasma bubbles (EPBs). Ionograms from the digisonde deployed at Shisanling are used to investigate the MSTID. Ionospheric parameters obtained from the ionograms include vertical virtual heights ($h'f$ and $h'E_s$) of F_2 and E_s layers, critical frequencies (f_oF_2 and f_oE_s) of F_2 and E_s layers, the average electron density <Ne> integrated from the ionospheric bottomside to the $h'f$ of 350 km, and the total electron content (TEC) recorded by the digisonde. The neutral wind at 250 km from the FPI deployed at Xinglong in April 2010 is also used to check its effect on the background ionosphere. The FPI instrument was developed by the National Center for Atmospheric Research and is similar in design to the one currently being used in Resolute Bay, Canada (Wu et al., 2004). Observations from these three instruments (ASAI, digisonde, and FPI) have been previously used to study the mesoscale field-aligned irregularity structures of airglow associated with a MSTID event by Sun et al. (2015). Photon numbers measured by the spectrometer deployed at Xinglong were also used to compare counts of airglow emission intensity from the airglow images. Rotational temperature of hydroxyl (OH) airglow emission measured by this spectrometer was previously used to compare with TIMED/SABER temperature by Liu et al. (2015).

3. Results

3.1. Special Midlatitudinal Airglow Event Observed by the ASAI

Airglow structures from the ASAI for the night of 9 August 2013 are shown in Figure 1. Figure 1a presents the raw airglow images during 13:40:07–18:40:37 universal time (UT). Note that the relationship between UT and local time (LT) at Xinglong is LT = UT + 7.84. In Figure 1a, we have mapped the raw airglow images in the geographic coordinate system by assuming that the airglow layer was at 250 km. At 13:40:07 UT, a cluster of airglow structures already appeared in the FoV of the ASAI. At least four depletions, which oriented from the northwest to the southeast, passed over Xinglong (red solid five-pointed star) and Shisanling (yellow solid triangle) stations in this night. The first two depletions appearing in stripes were marked with d_1 and d_2. Following the d_2 is a broader depletion region marked with d_3. It is difficult to identify the smaller-scale substructure of d_3 before 14:20:11 UT. Until 15:40:19 UT, the depletion d_3 seems to already split into two striped structures marked with d_{3a} and d_{3b}. Following the depletion d_3 is another one striped region marked with d_4, which became a bifurcation structure and surged poleward rapidly later on (e.g., 16:00:21 UT). Meanwhile, at least four airglow enhancements (marked as b_1, b_2, b_3, and b_4) appeared in this event. The enhancements of b_1 and b_4 already appeared at 15:40:19 UT and gradually evolved into the extremely bright airglow emission regions. They were generated within two adjacent depletions. The enhancement b_3 had extended poleward from lower than 35.0°N at 16:20:23 UT to over 45.0°N at 18:00:33 UT, and the poleward surged enhancement b_2 merged with the enhancement b_3, forming one bright region. Note that fast recombination of the airglow depletion occurred when the enhancements b_2 and b_3 were surging poleward. After 16:40:25 UT, the entire airglow structures became unclear. The left branch of bifurcation structure d_4 obviously disappeared at 17:00:27 UT. Movie S1 in the supporting information gives the detailed evolution process of this event.

Figure 1b further presents perturbation (%) airglow images during 13:40:07–18:40:37 UT. An 1.0-hr running mean was applied to obtain the airglow perturbation (%) field. Note that those two depletions d_{3a} and d_{3b} in Figure 1a actually have developed from the northeast and did not split from the depletion d_3. Moreover, some other airglow depletions also appeared at latitude higher than 45.0°N. The whole FoV of the ASAI is full of wave-like structures, which were oriented from northwest to southeast and propagate southwestward. Movie S2 in the supporting information clearly illustrates the evolution of these perturbations.

Characteristics of phase elongation and propagation of airglow structures described above are consistent with those nighttime MSTIDs as that previously reported by Sun et al. (2015) at Xinglong. Undoubtedly, airglow event showed in this study is evolved from the typical nighttime MSTID. Otsuka et al. (2012) previously reported an EPB event that extended poleward to encounter with a MSTID at near 25°N of geographic latitude in Japan. Our airglow observations at Fuke exclude this possibility. Movie S3 (630-nm airglow images at Fuke) in the supporting information clearly illustrates that several airglow depletions were oriented from northeast to southwest and propagated southeastward during 13:24:03–16:53:17 UT.

Presented in Figure 2 are the structured parameters of this event (Figure 2I) and the cross sections (keograms) of airglow images obtained at this night (Figures 2II and 2III). Figures 2I-a and 2I-b separately present the southwestward propagating velocity of each depletion in the direction passing through the zenith of Xinglong and the westward angle (positive westward) of each depletion with respect to the geographic north during 13:40:00–16:40:00 UT. Here note that airglow depletions after 16:40:00 UT became too unclear to obtain these two parameters accurately. We have divided displacement of the minimum airglow intensity location of each depletion with a time offset (about 15-min interval) to estimate the velocity. The westward angle is directly measured by a protractor. Figures 2II-a and 2II-b (Figures 2II-c and 2II-d) are the temporal variations of West-East (W-E) and North-South (N-S) cross sections (or keograms) in gray (jet) intensity to illustrate temporary evolution of depletions d_1–d_4 (enhancements b_1–b_4). With a width of 100 km, those W-E (N-S) cross sections of airglow images having a centered geographic latitude (longitude) of 40.4°N (117.6°E) were stacked to obtain the W-E (N-S) keogram. Ranges of those W-E and N-S cross sections are 104.0°–132.0°E and 31.0°–49.0°N, respectively. In order to illustrate the structured evolution more clearly, Figures 2III-a to 2III-d (Figures 2III-e to 2III-h) further present the W-E keograms of the airglow images in gray (jet) intensity at a centered geographic latitudes of 33.6°, 36.3°, 38.9°, and 41.6°N, respectively.

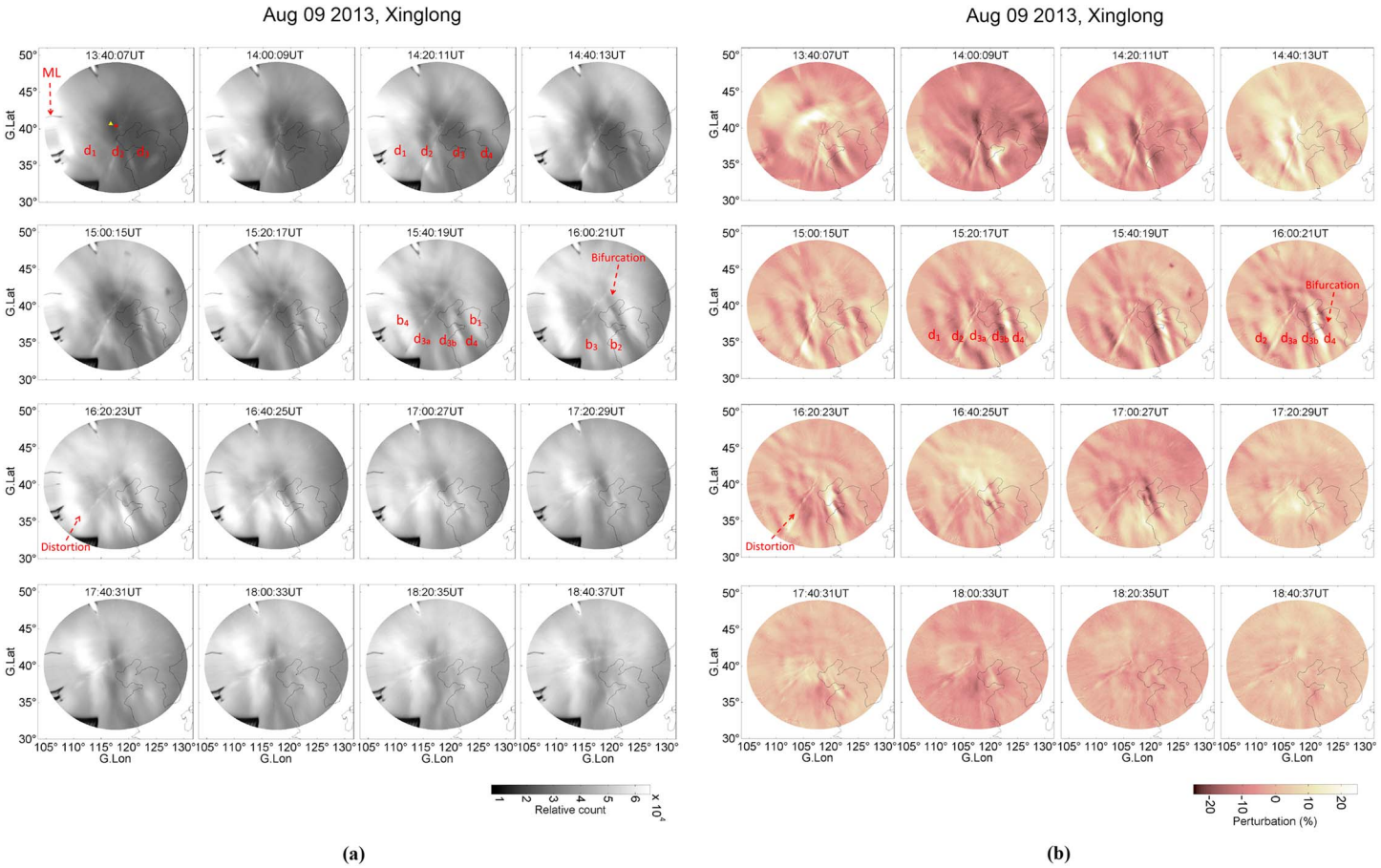

Figure 1. (a) Images (in 20-min cadence) of the medium-scale traveling ionospheric disturbance (MSTID) from 13:40:07 to 18:40:37 UT, at the night of 09 August 2013. The observed images were mapped onto geographical coordinate, by assuming that the airglow emission layer was at 250 km. The d_1-d_4 (including d_{3a} and d_{3b}) and b_1-b_4 are airglow depletions and enhancements we interest, respectively. The edge bright marked with ML is the moon light. (b) Airglow perturbation images of the MSTIDs from 13:40:07 to 18:40:37 UT. A perturbation image $\widehat{I}$can be obtained by expression $\widehat{I} = (I-\overline{I})/\overline{I}\times 100\%$, where I and $\overline{I}$ are a raw airglow image and an 1.0 hour running mean image of raw airglow images, respectively.

During 13:40:00–16:40:00 UT, the depletion velocity presented in Figure 2I-a is within the range of 6.0–225.0 m/s, with an averaged result (red line) varying from 50.0 to 115.0 m/s. Meanwhile, the westward angle of each depletion in Figure 2I-b has complicated variations with UT. Note that depletion d_4 rotated about 10° anticlockwise (from 10.0° to 20.0°) when it was bifurcated between 15:30:00 and 16:40:00 UT.

A complicated morphological evolution of airglow depletions and enhancements occurred after 16:00:00 UT. In Figure 2II-a, multilayer structures of airglow intensity variations appeared in d_4 during 16:30:00–19:30:00 UT. This characteristic of d_4 is caused by its bifurcation and can be also seen from Figures 2III-a to 2III-d. Distortions of d_{3a} and d_{3b} at geographic latitude of 40.4°N occurred from about 16:00:00 UT. During 16:00:00–18:00:00 UT, more severe distortions of d_3 and d_4 at geographic latitude of 36.3°N can be found in Figure 2III-b. Such distortions of d_{3a} and d_{3b} can be clearly seen at 16:20:23 UT in Figure 1a. From Figure 2II-c, the airglow enhancements b_1, b_3, and b_4 reversed their motion from west to east and then to west in some time spans at the geographic latitude of 40.4°N. Such a westward reversal of b_2 can be also seen from Figures 2III-e, 2III-f, and 2III-h and that of b_1 from Figures 2III-f and 2III-h at other selected geographic latitudes. In Figure 2II-d (also in Figure 2II-b), the enhancement b_2 also reversed its meridional motion from equatorward to poleward at about 16:00:00 UT at geographic longitude of 117.6°E. From the slope of the dotted line, the poleward velocity of enhancement b_2 is estimated about 99.5 m/s (3.1°/hr). Note that all depletions have an obviously westward motion before 17:00:00 UT. After 16:00:00 UT, westward velocities of the depletions decreased substantially. The d_4 almost stopped to move westward after 17:00:00 UT.

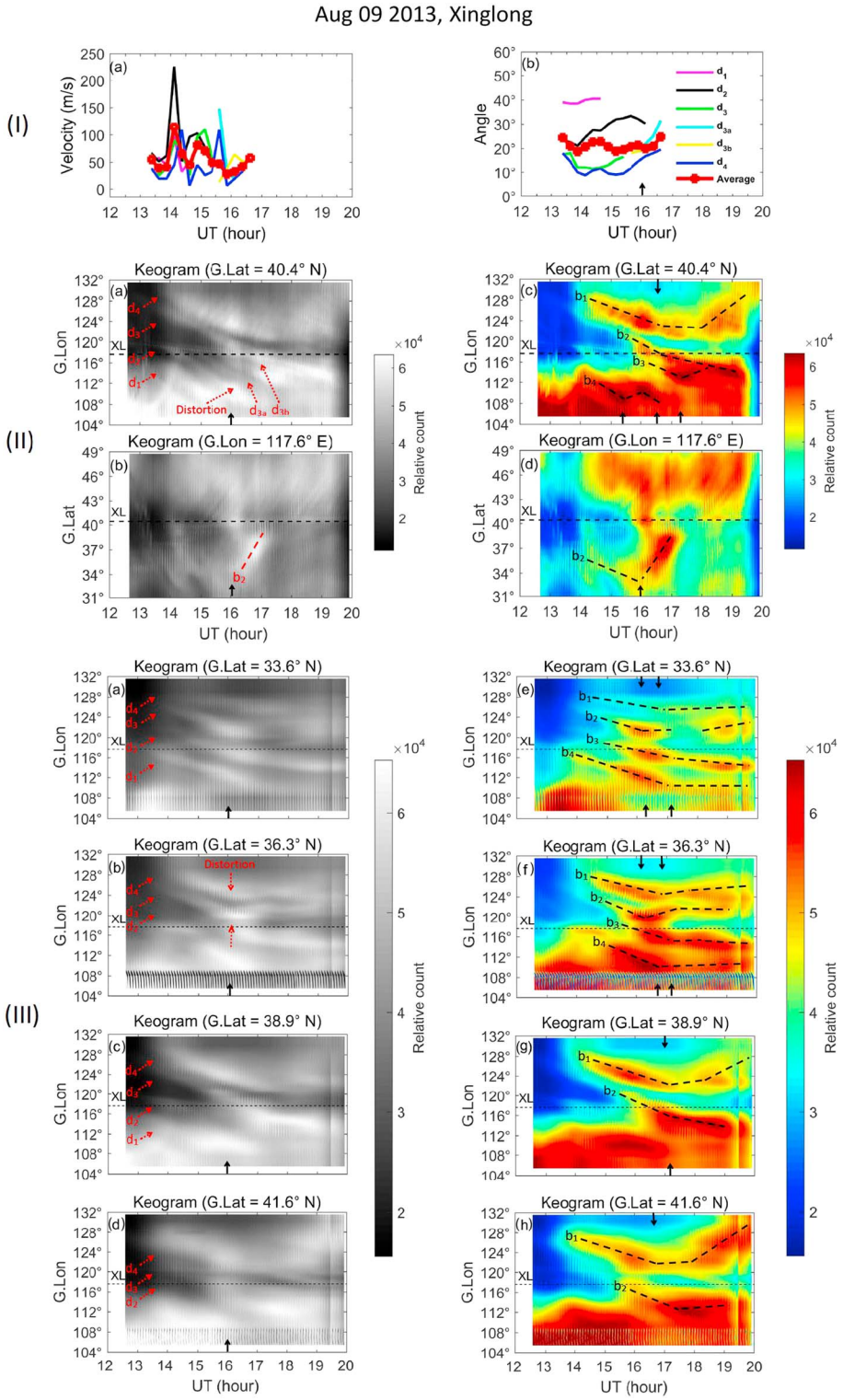

Figure 2. (I-a) Velocities of southwestward propagating depletions d_1, d_2, d_3, d_{3a}, d_{3b}, and d_4 in the direction passing through the zenith of Xinglong and their averaged velocity. (I-b) The westward angles (positive westward) of the phase elongations of depletions with respect to the geographic north and their averaged angle. 2II-a and 2II-b (2II-c and 2II-d), respectively, give the West-East and North-South sections (keograms) of the images in gray (jet) intensity at the geographic latitude and longitude of 40.4°N and 117.6°E, respectively. 2III-a to 2III-d (2III-e to 2III-h) give the West-East keograms of images at the geographic latitudes of 33.6°, 36.3°, 38.9°, and 41.6°N, respectively.

3.2. NPDE Observed by the Digisonde

Except for Figures 3I-d and 3I-e, other figures in Figure 3 present the ionospheric parameters obtained from ionograms in Shisanling during 10:00:00–22:00:00 UT on 9 August 2013. Figure 3I-a illustrates the vertical $h'f$ of the F_2 layer at 3.5, 4.0, 4.5, and 5.0 MHz and a minimum $h'f$ of the F_2 layer, and $h'E_s$ of the E_s layer. Figure 3I-b gives the f_oE_s and f_oF_2 of both E_s and F_2 layers. Figure 3I-c shows an average electron density <Ne> integrated from the ionospheric bottomside to the $h'f$ of 350 km by using a methodology described by Weber et al. (1980), and further used by Pimenta et al. (2004) and Sun et al. (2017). Figures 3I-f to 3I-h present the perturbation results of $h'f$, f_oF_2, and integrated TEC from the ionospheric bottomside to upside recorded by the digisonde, respectively. The green lines in Figures 3I-f to 3I-h represent perturbations of these parameters, which are obtained by subtracting the measurements on 9 August (the red lines) from the 10-day (5–14 August) mean values (the blue lines). Figures 3I-d and 3I-e give airglow counts at the zenith of the ASAI and the photon numbers recorded by the spectrometer, respectively. Note that a time span (about 15:30:00–17:15:00 UT) covered by the solid lines L1 and L2 in Figure 3I indicates a time range when this cluster of airglow depletions in Figure 1 was drastically evolving. Figures 3II-a to 3II-f further give the average counts of the airglow emission intensity within 10° to 60° FoVs of airglow images, respectively. Figures 3II-g to 3II-l give those results at the North and South (N and S) parts of the selected FoVs.

In Figure 3I-a, the vertical $h'f$ of the F_2 layer presents a large-scale perturbation at the vicinity of 300 km at this night. During 12:00:00–15:00:00 UT, the ionosphere was developing in an uplifted region with maximum $h'f$ of over 350 km. Subsequently, ionospheric $h'f$ decreased to about 250 km during 15:30:00–16:30:00 UT and then gradually increased to over 350 km at 19:30:00 UT. Note that the ionospheric $h'f$ was decreasing during the drastic evolution of this cluster of airglow depletions. From the perturbation structure in Figure 3I-f (the green lines), the maximum amplitude of the decreasing region reaches −50 km (positive upward).

The f_oF_2 in Figure 3I-b and its perturbation in Figure 3I-g (an increment of 1 MHz) increased slowly when the ionospheric height was decreasing. Compared with those at 13:00:00 UT (about 2.5×10^5 el/cm^{-3}), the <Ne> (in Figure 3I-c) estimated from the digisonde measurements showed an increment of about 1.5×10^5 el/cm^{-3} at 16:00:00 UT. When compared with the 10-day mean value (about 8 TECu), the perturbation of TEC in Figure 3I-h also increased by 3 TECu.

During 13:00:00–16:00:00 UT, the zenith airglow count and photon number in Figures 3I-d and 3I-e increased from 2.0×10^4 to 5.5×10^4 and from 2.0×10^8 to 5.5×10^8 photons/cm^2 nm s. A prominent peak of airglow emission intensity occurred at 16:00:00 UT. Such a peak of airglow emission intensity can be also seen in Figure 3-II clearly. This peak is still prominent even when the selected FoV of the image reaches 40°, which corresponds to a zenith distance of 207 km at 250 km.

Based on the analyses above, we present a special midlatitudinal airglow event that was drastically evolving during the occurrence of NPDE or NIAEI of the background ionosphere near midnight.

4. Discussions

Section 3 reports a midlatitudinal airglow event evolved from the typical nighttime MSTID. As a special example, this event is accompanied by a poleward surge of airglow depletion/enhancement and a bifurcation of depletion, during the occurrence of NPDE/NIAEI of the ionosphere near midnight. The NPDE/NIAEI occurred in an ionospheric descendant region with a reduced amplitude of 50 km.

Kelley et al. (2000) and Garcia, Kelley, Makela, Sultan, et al. (2000) previously reported this kind of special midlatitudinal airglow structures, and two of those events were caused by the geomagnetic storm. In the analyses of Garcia, Kelley, Makela, Sultan, et al. (2000), an eastward perturbation electric field induced by a geomagnetic storm most likely drives the high plasma density within EIA crest to interact with airglow depletions at midlatitudes, causing those poleward surge and bifurcation of airglow depletions. Aponte et al. (2000) further analyzed one of the events reported by Kelley et al. (2000) and obtained the same conclusion. However, the event we report here occurred at magnetically quiet time with the *Kp* index less than 2. New physical processes need to be proposed to explain this event.

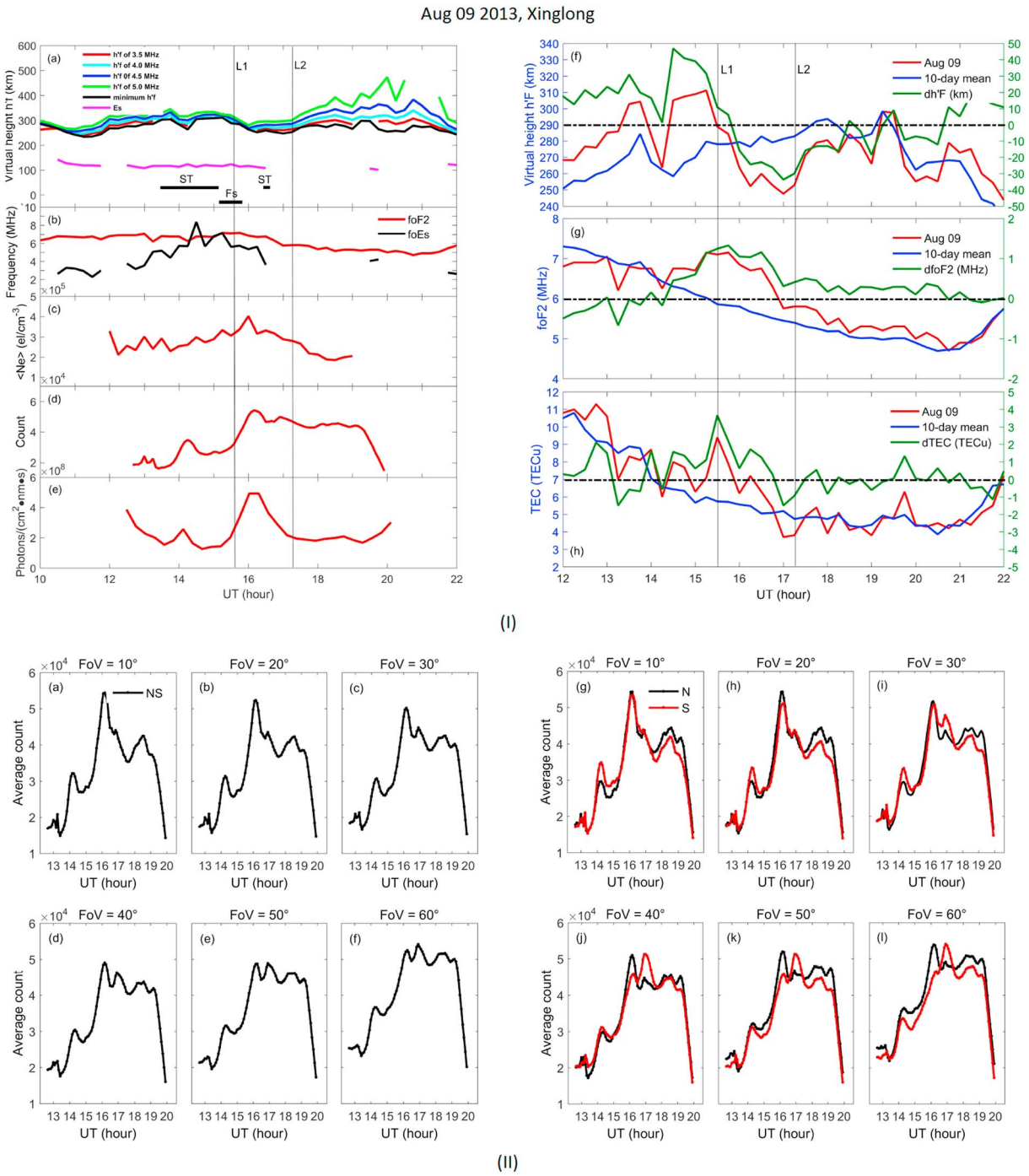

Figure 3. I-a to I-c gives the ionospheric $h'f$ of F_2 and E_s layers, f_oF_2 and f_oE_s, and the integrated electron density <Ne> from the ionospheric bottomside to the $h'f$ of 350 km, respectively. I-d gives the zenith airglow intensity counts from the Figure 1. I-e gives the photon numbers measured by the spectrometer. The red and blue lines in I-f to I-hr give the variations of the $h'f$, f_oF_2, and integrated total electron content (TEC) recorded by the digisonde from the ionospheric bottomside to upside on 9 August and the 10-day mean result (from 4 to 14 August), respectively. The green lines in I-f to I-h give the perturbation results on 9 August. The ST, E_s, and F_s in I-a and I-f represent the satellite traces, sporadic E, and spread F, respectively. II-a to II-f give the averaged counts of airglow emission intensity within ranges from 10° to 60° FoV of the airglow images. II-g to II-l give the results at the north (N) and south (S) parts of the selected FoVs.

What causes the quiet-time NPDE observed here? First, the quiet geomagnetic activity excludes the storm-time mechanisms proposed by Park (1971) and Shiokawa et al. (2002). Second, the mechanism of quiet-time NPDE that resulted from a large-scale TID as analyzed by Chen et al. (2018) seems also not appropriate. In Figures 3I-a or 3I-f, we indeed observed a large-scale perturbation of $h'f$ (with a

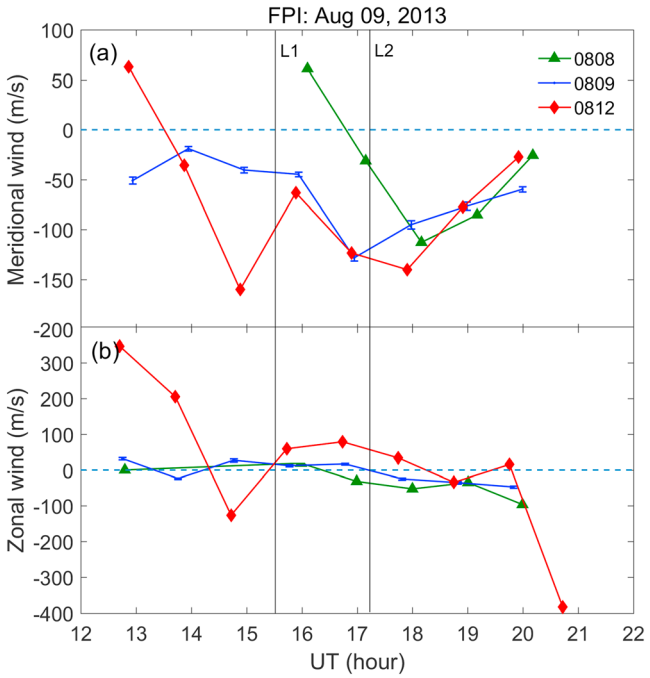

Figure 4. The neutral winds observed on 0808, 0809, 0812, August. The error bar on 0809 is also given. FPI = Fabry-Perot interferometer.

period of about 5 hr), which was accompanied by satellite trace—an ionogram signature for large-scale wave-like structures in the bottomside ionosphere (Narayanan et al., 2012; Tsunoda, 2008). However, the large-scale TID is usually associated with strong geomagnetic activity (Hunsucker, 1982). We further examine the mechanism of quiet-time NPDE induced by a westward electric field as proposed by Liu et al. (2013). In Figure 3I-f, the height of ionosphere continuously decreased by about 60 km during 14:30:00–17:00:00 UT (2.5 hr). The average vertical drift velocity of ionosphere is about −6.7 m/s (positive upward). First, we consider the effect of a meridional neutral wind on the vertical drift. Figure 4 gives the neutral wind observations during this night (the blue dotted line). A southward wind (positive north) in Figure 4a varies from about −50.0 to over −100.0 m/s when the ionospheric height decreases. The vertical plasma drift velocity (V) of the ionosphere caused by a meridional wind U is $U \times \cos(I) \times \sin(I)$, where I is the geomagnetic inclination (I = 57.7° in Xinglong). The observed southward wind (50.0–100.0 m/s) can thus cause a vertical upward drift velocity of about 22.6–45.2 m/s. Such a vertical upward drift must be balanced by other forces, such as a downward gravitational force or a westward electric field or both of them, to cause a downward motion of the ionosphere. The magnitude of the background electric field at magnetically quiet time is on the level of several tenths of 1.0 mV/m, which is smaller compared to the electric field from the F region dynamo at midlatitudes (e.g., Richmond et al., 1980; Otsuka et al., 2004, 2007, 2009). With a northern component of geomagnetic field (B_N) of 24,626.6 nT at 250 km in Xinglong, an eastward F region dynamo electric field ($U \times B_N \times \sin(I)$) with values of 1.0–2.0 mV/m can be caused by the southward U (50.0–100.0 m/s) in this event. Such an eastward electric filed will cause an upward motion of the ionosphere. Instead, the downward gravitational force will dominate the downward motion of ionosphere in this event. However, an upward pressure gradient force along the magnetic field line (e.g., Shiokawa et al., 2002) caused by the quiet-time NPDE would further balance the downward gravitational force. It is thus impossible for a westward electric field to determine the motion of the ionosphere here.

As analyzed above, the mechanisms proposed by Park (1971), Shiokawa et al. (2002), Liu et al. (2013), and Chen et al. (2018) fail to explain the observed NPDE well. However, we note that the observed NPDE here might be related to the MBW phenomena. In the airglow observations (e.g., Colerico & Mendillo, 2002), the MBW appears as a bright airglow region that is full of the most FoV of ASAI. It can propagate from the geographic equator to higher latitudes and cause a reversal/abatement in meridional neutral wind (Colerico & Mendillo, 2002). In our observations, the NPDE is accompanied with NIAEI that occupies a broad FoV of the ASAI (at least 40.0°). Reversals of westward motions of airglow enhancements b_1, b_2, and b_3 were observed. It is very possible that the MBW passed over the Xinglong in this night. When passing by the digisonde, the MBW can cause the NPDE or an increase of f_oF_2 in the F_2 layer and the associated NIAEI. Note that the southward neutral wind in Figure 4a stays almost the same value (near 50.0 m/s) at 15:00:00 UT and 16:00:00 UT and gradually increases to over 100 m/s at 17:00:00 UT. The passing-by MBW could have abated a portion of the southward wind during 15:00:00–16:00:00 UT in our event.

What causes the poleward surged bifurcation of airglow depletion? The formative process of such a bifurcation of airglow depletion should be similar to those in Kelley et al. (2000) and Garcia, Kelley, Makela, Sultan, et al. (2000). Here we propose the SGDI as a very possible mechanism to cause bifurcation of airglow depletion. When this airglow depletion of MSTID (with low plasma density) were encountered by the NPDE, an eastward polarization electric field would be generated to maintain the continuity of the field-line integrated ionospheric current $\mathbf{J}$ ($\nabla \bullet \mathbf{J} = 0$) and results in the poleward surge of the airglow depletion. The bifurcation would be generated by the SGDI when the eastward polarization electric field works on a northward sharp plasma gradient co-determined by the passing low plasma density within the airglow depletion of MSTID and the NPDE.

What causes the poleward surged airglow enhancements b_2 and b_3? Morphology of these two airglow enhancements looks like one of the plasma blobs (plasma density enhancements) associated with the EPBs as first reported by Pimenta et al. (2004, 2007). This kind of airglow enhancements is generated within adjacent airglow depletions. Plasma blobs are usually generated near or within EIA crests and previously explained as a combination result of plasma dynamic process associated with EPB formation and the equatorial anomaly fountain effect (e.g., Pimenta et al., 2004). However, the enhancements b_2 and b_3 here began to evolve at several degrees poleward of the anomaly crest (near 25° geographic latitude). Moreover, the northern EIA crest usually moves southward at nighttime (e.g., Narayanan et al., 2014, 2016; Sun et al., 2017). The proposed mechanism of plasma blob obviously fails to explain the airglow enhancements b_2 and b_3 here. From Figure 1a, one should note that the poleward surged airglow enhancements b_2 and b_3 were generated when the bifurcation of d_4 was evolving simultaneously. Moreover, morphological distortions of some airglow depletions and reversals of westward motions of some airglow enhancements simultaneously occurred. We suspect that the airglow enhancements b_2 and b_3 are part of NIAEI associated with the NPDE or the ramifications of interaction between the NPDE and the airglow depletions of MSTID. Note that the poleward surge of the airglow enhancement cannot be explained by the SGDI. The SGDI would be triggered when the plasma moves along the direction of the density gradient (Kelley, 1989). Because the plasma density inside the airglow enhancements b_2 and b_3 is higher than the surrounding structures, there must be a southward plasma density gradient in the opposite direction of the poleward propagation of MSTID.

5. Summaries

This paper presents observational evidence that the midlatitudinal special airglow event can be suggested as an interactive result of passing-by MSTID and the NPDE possibly associated with a MBW at magnetic quiet time. The poleward surged airglow depletion/enhancement and bifurcation structures were drastically generated in a gradually decreasing region of ionosphere accompanied by NPDE and NIAEI. The poleward surged airglow enhancement evolved within two adjacent depletions of midlatitudinal MSTID has been firstly reported in this study. We suggest that the poleward surge of depletion is attributed to an eastward electric field and the bifurcation of depletion is attributed to the SGDI, in which the plasma density gradient is codetermined by the depletion of MSTID and the NPDE.

Acknowledgments
This work was supported by the National Natural Science Foundation of China (41831073 and 41804146), the Open Research Project of Large Research Infrastructures of CAS —"Study on the interaction between low/midlatitude atmosphere and ionosphere based on the Chinese Meridian Project." This paper was also supported by the Specialized Research Fund for State Key Laboratories and the Strategic Priority Research Program of Chinese Academy of Sciences (XDA17010301 and XDA17010302). We acknowledge the use of ASAI, FPI, and spectrometer data from the Chinese Meridian Project (http://data.meridianproject.ac.cn/). The digisonde data were provided by the Institute of Geology and Geophysics, Chinese Academy of Sciences.

References

Aponte, N., González, S. A., Kelley, M. C., Tepley, C. A., Pi, X., & Iijima, B. (2000). Advection of the equatorial anomaly over Arecibo by small-storm related disturbance dynamo electric fields. *Geophysical Research Letters*, *27*(18), 2833–2836. https://doi.org/10.1029/2000GL000025

Chen, G., Wang, J., Zhang, S., Deng, Z., Zhong, D., Wu, C., et al. (2018). Opposite latitudinal dependence of the premidnight and postmidnight oscillations in the electron density of mid-latitude *F* layer. *Journal of Geophysical Research: Space Physics*, *123*, 796–807. https://doi.org/10.1002/2017JA024162

Colerico, M., & Mendillo, M. (2002). The current state of investigations regarding the thermospheric midnight temperature maximum (MTM). *Journal of Atmospheric and Solar - Terrestrial Physics*, *64*(12-14), 1361–1369. https://doi.org/10.1016/S1364-6826(02)00099-8

Colerico, M., Mendillo, M., Nottingham, D., Baumgardner, J., Meriwether, J., Mirick, J., et al. (1996). Coordinated measurements of *F* region dynamic related to the thermospheric midnight temperature maximum. *Journal of Geophysical Research*, *101*(A12), 26,783–26,793. https://doi.org/10.1029/96JA02337

Garcia, F. J., Kelley, M. C., Makela, J. J., & Huang, C.-S. (2000). Airglow observations of mesoscale low-velocity traveling ionospheric disturbances at midlatitudes. *Journal of Geophysical Research*, *105*(A8), 18,407–18,415. https://doi.org/10.1029/1999JA000305

Garcia, F. J., Kelley, M. C., Makela, J. J., Sultan, P. J., Pi, X., & Musman, S. (2000). Mesoscale structure of the mid-latitude ionosphere during high geomagnetic activity: Airglow and GPS observations. *Journal of Geophysical Research*, *105*(A8), 18,417–18,427. https://doi.org/10.1029/1999JA000306

Hunsucker, R. D. (1982). Atmospheric gravity waves generated in the high-latitude ionosphere: A review. *Reviews of Geophysics*, *20*(2), 293–315. https://doi.org/10.1029/RG020i002p00293

Kelley, M. C. (1989). *The Earth's ionosphere*. San Diego, CA: Academic.

Kelley, M. C., Makela, J. J., Swartz, W. E., Collins, S. C., Thonnard, S., Aponte, N., & Tepley, C. A. (2000). Caribbean ionosphere campaign, year one: Airglow and plasma observations during two intense mid-latitude spread-*F* events. *Geophysical Research Letters*, *27*(18), 2825–2828. https://doi.org/10.1029/2000GL000022

Liu, L., Chen, Y., Le, H., Ning, B., Wan, W., Liu, J., & Hu, L. (2013). A case study of post midnight enhancement in *F* layer electron density over Sanya of China. *Journal of Geophysical Research: Space Physics*, *118*, 4640–4648. https://doi.org/10.1002/jgra.50422

Liu, W., Xu, J., Smith, A. K., & Yuan, W. (2015). Comparison of rotational temperature derived from ground-based OH airglow observations with TIMED/SABER to evaluate the Einstein coefficients. *Journal of Geophysical Research: Space Physics*, *120*, 10,069–10,082. https://doi.org/10.1002/2015JA021886

Narayanan, V. L., Gurubaran, S., Shiokawa, K., & Emperumal, K. (2016). Shrinking equatorial plasma bubbles. *Journal of Geophysical Research: Space Physics*, *121*, 6924–6935. https://doi.org/10.1002/2016JA022633

Narayanan, V. L., Shiokawa, K., Otsuka, Y., & Saito, S. (2014). Airglow observations of nighttime medium-scale traveling ionospheric disturbances from Yonaguni: Statistical characteristics and low-latitude limit. *Journal of Geophysical Research: Space Physics*, *119*, 9268–9282. https://doi.org/10.1002/2014JA020368

Narayanan, V. L., Taori, A., Patra, A. K., Emperumal, K., & Gurubaran, S. (2012). On the importance of wave-like structures in the occurrence of equatorial plasma bubbles: A case study. *Journal of Geophysical Research*, *117*, A01306. https://doi.org/10.1029/2011JA017054

Otsuka, Y., Onoma, F., Shiokawa, K., Ogawa, T., Yamamoto, M., & Fukao, S. (2007). Simultaneous observations of nighttime medium-scale traveling ionospheric disturbances and *E* region field-aligned irregularities at midlatitude. *Journal of Geophysical Research*, *112*, A06317. https://doi.org/10.1029/2005JA011548

Otsuka, Y., Shiokawa, K., & Ogawa, T. (2012). Disappearance of equatorial plasma bubble after interaction with mid-latitude medium-scale traveling ionospheric disturbance. *Geophysical Research Letters*, *39*, L14105. https://doi.org/10.1029/2012GL052286

Otsuka, Y., Shiokawa, K., Ogawa, T., & Wilkinson, P. (2004). Geomagnetic conjugate observations of medium-scale traveling ionospheric disturbances at midlatitude using all-sky airglow imagers. *Geophysical Research Letters*, *31*, L15803. https://doi.org/10.1029/2004GL020262

Otsuka, Y., Shiokawa, K., Ogawa, T., Yokoyama, T., & Yamamoto, M. (2009). Spatial relationship of nighttime medium-scale traveling ionospheric disturbances and *F* region field-aligned irregularities observed with two spaced all-sky airglow imagers and the middle and upper Atmosphere radar. *Journal of Geophysical Research*, *114*, A05302. https://doi.org/10.1029/2008JA13902

Park, C. G. (1971). Westward electric fields as the cause of nighttime enhancements in electron concentrations in midlatitude *F* region. *Journal of Geophysical Research*, *76*(19), 4560–4568. https://doi.org/10.1029/JA076i019p04560

Pimenta, A. A., Sahai, Y., Bittencourt, J. A., Abdu, M. A., Takahashi, H., & Taylor, M. J. (2004). Plasma blobs observed by ground-based optical and radio techniques in the Brazilian tropical sector. *Geophysical Research Letters*, *31*, L12810. https://doi.org/10.1029/2004GL020233

Pimenta, A. A., Sahai, Y., Bittencourt, J. A., & Rich, F. J. (2007). Ionospheric plasma blobs observed by OI 630 nm all-sky imaging in the Brazilian Tropical sector during the major geomagnetic storm of April 6–7, 2000. *Geophysical Research Letters*, *34*, L02820. https://doi.org/10.1029/2006GL028529

Richmond, A. D., Bianc, M., Emery, B. A., Wand, R. H., Fejer, B. G., Woodman, R. F., et al. (1980). An empirical model of quiet-day ionospheric electric fields at middle and low latitudes. *Journal of Geophysical Research*, *85*(A9), 4658–4664. https://doi.org/10.1029/JA085iA09p04658

Shiokawa, K., Otsuka, Y., Ogawa, T., Balan, N., Igarashi, K., Ridley, A. J., et al. (2002). A large-scale traveling ionospheric disturbance during the magnetic storm of 15 September 1999. *Journal of Geophysical Research*, *107*(A6), 1088. https://doi.org/10.1029/2001JA000245

Sun, L., Xu, J., Wang, W., Yuan, W., & Zhu, Y. (2017). Evolution processes of a group of equatorial plasma bubble (EPBs) simultaneously observed by ground-based and satellite measurements in the equatorial region of China. *Journal of Geophysical Research: Space Physics*, *122*, 4819–4836. https://doi.org/10.1002/2016JA023223

Sun, L., Xu, J., Wang, W., Yue, X., Yuan, W., Ning, B., et al. (2015). Mesoscale field-aligned irregularity structures (FAIs) of airglow associated with medium-scale traveling ionospheric disturbances (MSTIDs). *Journal of Geophysical Research: Space Physics*, *120*, 9839–9858. https://doi.org/10.1002/2014JA020944

Tsunoda, R. T. (2008). Satellite traces: An ionogram signature for large-scale wave structure and a precursor for equatorial spread F. *Geophysical Research Letters*, *35*, L20110. https://doi.org/10.1029/2008GL035706

Wang, C. (2010). New chains of space weather monitoring stations in China. *Space Weather*, *8*, S08001. https://doi.org/10.1029/2010SW000603

Weber, E., Buchau, J., & Moore, J. (1980). Airborne studies of equatorial *F* layer ionospheric irregularities. *Journal of Geophysical Research*, *85*(A9), 4631–4641. https://doi.org/10.1029/JA085iA09p04631

Wu, Q., Gablehouse, R. D., Solomon, S. C., Killeen, T. L., & She, C. Y. (2004). A new Fabry-Perot interferometer for upper atmospheric research. *Proceedings of SPIE*, *5660*, 218–227. https://doi.org/10.1117/12.573084